Clay Delamination in Clay/Poly(Dicyclopentadiene) Nanocomposites Quantified by Small Angle Neutron Scattering and High-Resolution Transmission Electron Microscopy

Mitra Yoonessi,[†] Hossien Toghiani,[†] Tyrone L. Daulton,[‡] Jar-Shyong, Lin,[¥] and Charles U. Pittman Jr.*,[⊥]

Dave C. Swalm School of Chemical Engineering and Department of Chemistry, Mississippi State University, Mississippi State, Mississippi 39762, Oak Ridge National Laboratory, Oak Ridge, Tennessee 37831, and Naval Research Laboratory, Marine Geosciences Division, Stennis Space Center, Mississippi 39529

Received July 2, 2004; Revised Manuscript Received September 18, 2004

ABSTRACT: Highly delaminated clay/poly(dicyclopentadiene) nanocomposites were prepared by in-situ, ring-opening metathesis polymerization of presonicated mixtures of the liquid dicyclopentadiene (DCPD) and organically modified Montmorillonite clays. Three nanocomposite series (using Montmorillonites: I-28, I-44pa) of increasing clay loadings (0.5, 1.0, and 2.0 wt%) and modified Montmorillonite PGW (0.5 wt%) were synthesized. The dispersed microstructure of the clays in the nanocomposites was characterized by small-angle neutron scattering (SANS), ultra-small-angle neutron scattering (USANS), small-angle X-ray scattering (SAXS), and high-resolution transmission electron microscopy (HR-TEM). All clays were highly delaminated and well dispersed within their host matrixes. The mean number of individual clay platelets per tactoid was predicted by fitting SANS data to the stacked-disk model and measured directly from HR-TEM images of a large number of tactoids in each sample. SANS results were in good agreement with HR-TEM for composites with low clay concentrations (0.5 wt%); however, deviations were observed at higher clay loadings (2.0 wt%). These deviations are discussed in terms of several factors not taken into account by the stacked-disk model: (a) long-range interactions, which become more important at high loadings; (b) departure of tactoid geometries from parallel stacks of rigid disks; and (c) the polydispersity of tactoid thicknesses. SAXS peaks were not present for most of the synthesized nanocomposites, suggesting a high degree of clay delamination was achieved. However, a broad peak was observed for the 2.0 wt% I-44pa clay nanocomposite, indicating the presence of some larger tactoids than in the other nanocomposites having a range of *d*-spacings. The HR-TEM measured distributions of clay platelet *d*-spacings in tactoids dispersed within the nanocomposites which were in the range from 8 to 20 Å (12−15 Å average), indicating that the quaternary ammonium ion pillaring agents were no longer present. These quaternary salts either decomposed during the high-temperature (260 °C) stage of curing or were not fully exchanged with the interlayer cations present between all platelet interlayers during the original clay modification. Clay/polyDCPD composites were also prepared using PGW clay modified by poly(ethylene glycol). This clay dispersed more rapidly, needing less sonication than the other clays. The resistance to delamination of all nanocomposites studied increased with greater clay loading under equivalent synthesis conditions.

Introduction

Montmorillonite clay has long been used as filler and reinforcing agent[1] in polymer systems because of its availability and low cost. The improvements in physical/mechanical properties of polymers upon forming composites with clays is highly dependent on the degree of clay dispersion.[1] In contrast to micrometer-sized particles used in conventional composites,[2] clays can be delaminated into tens-of-nanometer-thick grain (tactoid) sizes and a portion even into individual 1 nm thick platelets. Toyota researchers demonstrated that small amounts of well-exfoliated organically modified clay improves mechanical, barrier, and thermal properties, as well as flame resistance of Nylon 6.[3−6] Dispersion of clay into other polymer matrixes, including epoxy resins,[7−9] silicon elastomers,[2] and polyethers[10] has been investigated. In particular, dicyclopentadiene (DCPD), a low-viscosity monomer that can be polymerized to a highly cross-linked polymer network, has been used to form clay nanocomposites.[11] Organically-modified Montmorillonite in polyDCPD composites, prepared by sonicating the clay in DCPD, were shown to be highly delaminated by X-ray diffraction, confocal laser microscopy, and transmission electron microscopy (TEM).[11]

Unmodified and organically modified clays in clay/solvent and clay/water-soluble polymer/aqueous systems have been well examined by other researchers.[12−22] However, few attempts have been made to investigate polymer/clay nanocomposites by scattering techniques, and no scattering studies coupled with high-resolution (HR)-TEM have been attempted. Small-angle neutron scattering (SANS) and small-angle X-ray scattering (SAXS) are powerful techniques for studying the micro- and nano-domain structures of polymer systems, fillers, and particles.[17,18] Both techniques exhibit high sensitivity to structural features on length scales of 1−100 nm. Consequently, SANS and SAXS can be used to study phase dispersion in matrixes, polymerization, emulsification, colloid stabilization, shear-induced structures,

* Corresponding author. Tel: 662-325-7616. Fax: 662-325-7611. E-mail: cpittman@ra.msstate.edu.
[†] Dave C. Swalm School of Chemical Engineering, Mississippi State University.
[⊥] Department of Chemistry, Mississippi State University.
[¥] Oak Ridge National Laboratory.
[‡] Naval Research Laboratory.

10.1021/ma048663e CCC: $30.25
Published on Web 01/07/2005

and phase domain behavior in polymers.[18] Furthermore, differences in the manner by which X-rays and neutrons scatter in solids enables complementary contrast variation, especially in multicomponent materials with ordered structures.[18] Compared to neutron and X-ray scattering techniques, HR-TEM provides detailed microstructural information of localized areas on the 0.2 nm spatial scale. Heterogeneous microstructures (as present in nanocomposites) can be characterized by HR-TEM by examining a large number of representative regions, allowing the comparison of results from HR-TEM and scattering techniques.

In this paper, polyDCPD/clay nanocomposites,[11] using three different Montmorillonites, were synthesized by stirring clay into the low-viscosity monomer, DCPD, followed by sonication to delaminate the clays and then in-situ DCPD ring-opening metathesis polymerization. The nature of the clay delamination in the clay/polyDCPD nanocomposites was characterized using a combination of SANS,[19] ultra-small-angle neutron scattering (USANS), SAXS, and HR-TEM. We show all clays were highly delaminated in the nanocomposites. Further, SANS data on these composites were fitted to the stacked-disk model developed[17−22] by Glinka,[19a] Hanley et al.,[20,21] and Ho et al.[17,22] Model predictions based on SANS data for the mean number of individual clay platelets per tactoid were compared to a large number of direct HR-TEM measurements, providing the first experimental test of the stacked-disk model as applied to clay nanocomposites.

Experimental Section

Clay Material. Modified Montmorillonite clays (Nanomer**:** I-28 and I-44pa and PGW), were provided by Nanocor, Inc. $(M^{+}_{0.374}(Al_{1.626}(Mg{+}Fe)_{0.374})Si_4O_{10}(OH)_2{\cdot}nH_2O$ (where M^+ is an exchangeable cation) was obtained from elemental analysis for the precursor clay prior to organic modification. Both I-28 and I-44pa are organically modified and were used in this work as-received. The organic modifier in I-28 is the trimethyldodecadecylammonium ion, and the modifier in I-44pa is the dimethyldidecylammonium ion. These ammonium ions were exchanged into the clay from their chloride salts by Nanocor, Inc. Both I-28 and I-44pa clays were characterized with XRD to have *d*-spacings of 2.56 nm; however, we measured *d*-spacings of 2.25 nm (I-28) and 3.2 nm (I-44pa) by SAXS. The *d*-spacings measured by XRD and SAXS can differ by ∼10−20% due to higher sensitivity of the SAXS detector at the small angles. The as-received PGW clay exhibited a *d*-spacing of 2.31 nm by SAXS. As-received PGW was treated with dimethyldidecylammonium bromide (a further ion exchange) and then with poly(ethylene glycol) (PEG), $M_w = 900$. The *d*-spacing of PEG-modified PGW increased from its initial as-received value of 2.31 to 3.2 nm (SAXS) after treatment.

PGW clay modification was conducted as follows. PGW clay (10 g) was dispersed in deionized water (333 g) overnight, and the following day, 2.71 g of PEG was added to the dispersion. After being stirred for 10 min, dimethyldidecylammonium bromide (5.34 g) was added and the temperature was increased to 55 °C. This dispersion was stirred for another 20 min and then filtered. The modified clay was washed several times with deionized water to remove residual PEG/surfactant, filtered, and allowed to dry.[15,16]

Preparation of Nanocomposites. A series of dispersions for each clay (I-28, I-44pa, and PEG-modified PGW) with 0.5, 1.0, and 2.0 wt% were prepared by adding each clay, individually, into the liquid monomer (96:4 mixture of DCPD and cyclopentadiene (CPD)) at room temperature with thorough mixing. DCPD (99.2% purity), under the trade name Ultrene99, was obtained from Cymetech, LLC. CPD was produced by thermal cracking of DCPD followed by rapid quenching. It was added to DCPD to lower the melting point (39 °C for pure DCPD) of the monomer to well below room temperature. These clay/DCPD mixtures (10 g) were then sonicated using a 20 kHz 500 W ultrasonic processor ModelGE501 (Ace Glass) for 3 h (I-28 clay/DCPD and I-44pa/DCPD) but only 10 min for PEG-modified PGW/DCPD. Highly delaminated clay nanocomposites were formed, following sonication, by catalyst addition and in-situ polymerization of the highly delaminated clay/monomer dispersions. The catalyst used to cure DCPD was dichloro(3-methyl-2-butenylidene)-bis-tricyclopentylphosphineruthenium (a Grubbs-type catalyst), provided by Cymetech, LLC. However, it was not possible to form DCPD nanocomposites using PEG-modified PGW at loads above 0.5 wt% because residual bromide ions, from the dimethyldidecylammonium bromide exchange step, deactivated the ruthenium complex ring-opening polymerization catalyst. Full details of these preparations have been previously reported.[11]

Characterization Methods. *X-Ray Photoelectron Spectroscopy (XPS).* XPS experiments were performed on a Physical Electronics PHI Model 1600 surface-analysis system. This instrument was equipped with a PHI 10-360 spherical capacitor energy analyzer (SCA) fitted with an Omni Focus III small-area lens (800 μm diameter analysis area) and a high-performance multichannel detector. The electron take-off angle was 30°.[24,25] XPS spectra were obtained using an achromatic Mg Kα (1253.6 cm^{-1}) X-ray source operated at 200 W. Survey scans were collected from 0 to 1100 eV. High-resolution scans were performed with a pass energy adjusted to 23.5 eV. The vacuum-system pressure was maintained at approximately 10^{-9} Torr during all XPS experiments.

Nonlinear least squares curve fitting software (Spectral Data Processor, version 2.3) with a Gaussian−Lorentzian function and Shirely background subtraction was used to deconvolute the XPS peaks. A Lorentz/Gaussian mix of 60:40 was used. The carbon 1s electron binding energy corresponding to graphitic carbon was referenced at 284.6 eV for calibration.[25,26a,b] The energy resolution of the spherical capacitance analyzer, determined from the full-width half-maximum (fwhm) of the $4f_{7/2}$ core peak of gold foil, was 1.07 eV. Atomic ratios were calculated from the XPS spectra after correcting the relative peak areas by sensitivity factors based on transmission characteristics of the Physical Electronics SCA PHI 10-360.[24,25,27]

Small-Angle Neutron Scattering. SANS experiments were performed using the NG-3 30m SANS instrument at the National Institute of Standards and Technology (NIST) Center for Neutron Research (NCNR).[28] A monochromatic beam of neutrons with a wavelength of $\lambda = 6$ Å and resolution of $\Delta\lambda/\lambda = 0.11$ was used. The monochromatic beam was collimated by circular pinhole irises in a 15 m long evacuated presample flight path. The postsample flight path consists of a long cylindrical section that forms a vacuum enclosure for a large two-dimensional (2D) position-sensitive detector. The area detector (64 × 64 cm^2 with a 0.5 cm fwhm spatial resolution) moves along rails, parallel to the neutron beam, inside the cylindrical vessel to vary the sample-to-detector distances from 1.3 to 13.2 m. The detector moves transversely to the beam direction (by up to 30 cm) to extend the q range covered at a given detector distance.[29,30] The term q is the modulus of the scattering vector, or the magnitude of momentum transfer ($q = (4\pi/\lambda)\sin(\theta/2)$; where λ is the radiation wavelength of X-ray or neutrons, and θ is the scattering angle).Two sample-to-detector distances of 2 and 13 m were used covering the q range 0.003−0.3 $Å^{-1}$. The samples (held at room temperature) were mounted by tape on a 10-position sample holder controlled by instrument-control software. Scattered intensities were reduced and corrected for the transmission, background, and parasitic scattering using Igor pro version 4.07 software, from Wavematrics, Inc. The 2-D data was then circularly averaged to produce a one-dimensional graph of scattering intensity, $I(q)$, as a function of the wave vector, q, where $q = (4\pi/\lambda)\sin(\theta/2)$ and θ is the scattering angle.[31]

Ultra-High-Resolution Small-Angle Neutron Scattering. USANS experiments were performed using the BT5 perfect-crystal diffractometer (PCD) instrument at the NIST NCNR. The PCD greatly extends the experimental capability to allow

the observation of micrometer-sized structural features.The PCD increases the maximum size of features which were accessible with the NCNR's 30 m long, pinhole collimation SANS instruments by nearly 2 orders of magnitude, from $\sim 10^2$ to 10^4 nm.[32a] The PCD is a Bonse−Hart-type instrument with a pair of large triple-bounce, channel-cut silicon (220) crystals serving as monochromator and analyzer, respectively. The perfect crystals provide high angular resolution, while the multiple reflections suppress the "wings" of the beam profile. This improves the signal-to-noise ratio to values comparable to that obtained by pinhole instruments. This technique, widely utilized for X-rays for many years, has only recently been successfully adapted for neutrons,[32a,b,c] as dynamical diffraction effects arising from the deep penetration of neutrons in thick, perfect crystals has become understood.[32b] The q range of this instrument is 0.00005 to $\sim$0.01 Å^{-1}, which probes the size regime of 0.1 to ~ 10 μm.[32a,b,c]

Small-Angle X-Ray Scattering. Two SAXS instruments were used in order to cover a wide q range. The same composite sample (from each series) was examined with both instruments. The first experiments were performed on Oak Ridge National Laboratory's 10-m SAXS instrument.[33,34] The instrument is equipped with a 12 Kw Rigaku roatating-anode X-ray generator, a pyrolytic graphite monochromator, and a two-dimensional position-sensitive area detector of 20 × 20 cm^2 with a resolution of 64 × 64 virtual pixels. Cu Kα radiation (λ = 1.542 Å) was used and the sample-to-detector distance was 1.119 m. Corrections were made for instrumental background (dark current due to both cosmic radiation and electronic noises in the detector circuitry) and detector nonuniformity/efficiency on a cell-by-cell basis (using an Fe^{55} radioactive isotope standard, which emits X-rays isotropically by electron capture). The data were radially (azimuthally) averaged in the q range, $0.01 < q < 0.4$ Å^{-1}, $q = (4\pi/\lambda)\sin(\theta/2)$, where λ is the X-ray wavelength, and θ is the scattering angle. The data were then converted to an absolute differential scattering cross section by means of precalibrated secondary standards.[35] The absolute scattering intensity is in cm^{-1} units.

The second SAXS instrument was a Molecular Metrology Small-Angle X-ray Scattering System at the University of Tennessee, Knoxville with a sample-to-detector distance of 0.5 m. The X-ray source was the Cu, Kα (λ = 1.542 Å) radiation from a sealed tube, micro-focused by a pair of Kirkpatrick−Baez multilayered focusing mirrors, and the operating X-ray power was only 45 kV and 0.66 mA. A Gabriel-type 2-D circular detector of 12.5 cm in diameter was used. A cathode-encoding scheme for radiation event position sensing provided a high resolution of 1024 × 1024 pixels for data acquisition for the detector. The data were radially averaged and converted to an absolute intensity unit of cm^{-1}, yielding the intensity of scattering versus scattered wave vector q.

Transmission Electron Microscopy. Nanocomposites were ultramicrotomed with Reichert−Jung Ultracut E ultramicrotomes using a diamond knife at room temperature, providing sections with nominal thicknesses of 70−85 nm. Microtomed slices were mounted on Formvar or amorphous-carbon-coated copper TEM grids. The contrast between the dispersed clays and polymer matrix was sufficient for imaging without staining.

A JEOL JEM-100CX II 80 kV transmission electron microscope was used to study the dispersion of the clay layers and tactoids. HR-TEM imaging was performed using a JEOL JEM-3010 analytical transmission electron microscope at the Naval Research Laboratory, Stennis Space Center, operating at 300 kV with a LaB_6 filament, an EM-30022HT pole piece, and a measured point-to-point resolution of 2.1 Å. The HR-TEM instrument is equipped with a side-entry motorized five-axes goniometer, a Noran energy-dispersive X-ray spectroscopy (EDS) system, a Gatan 764 multiscan camera (MSC), and a Gatan imaging filter (GIF200). All HR-TEM images were recorded on film at 250k × magnification using a 60 μm objective aperture.

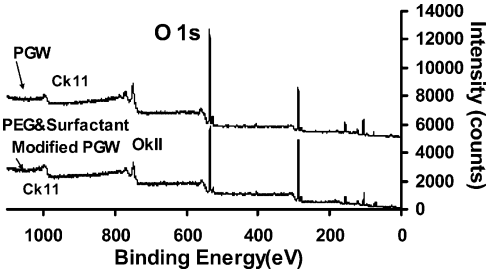

Figure 1. X-ray photoelectron spectra of as-received PGW clay versus poly(ethylene glycol) (M_w = 900)-modified PGW clay, which was pretreated with dimethyldidecylammonium bromide.

Results and Discussion

XPS Study of PGW Clay Modification. The surfaces of the PGW clay platelets were modified using both PEG and dimethyldidecylammonium bromide. The exchange reaction replaces interlayer cations with dimethyldidecylammonium ions. In the process, molecules containing −OH, $-NH_2$, and $-NH_3^+$ or $-NR_3^+$ functions can be adsorbed to clay platelet surfaces by hydrogen bonding, van der Waals interactions, and Coulombic attractions (in the case of $-NH_3^+$ and $-NR_3^+$).[36] Adsorption of PEG to platelet surfaces or into ammonium ion-pillared galleries might be promoted by dipole, van der Waals, and hydrogen bonding interactions.[15,16] XPS analysis of the as-received PGW clay indicated the presence of Al, Si, C, N, and O. The presence of N in this alumina-silicate-layered clay indicates that prior alkylammonium ion exchange had been performed (Figure 1). An XPS scan of PEG-modified PGW indicates the presence of Al, Si, O, C, N, and Br. The atomic compositions (atom percents) of Al, Si, and O (from alumina-silica sheets), decreased from 5.6, 7.1, and 45.5% to 3.4, 5.5, and 32.1%, respectively, after PEG modification. There was no change in the alumina-silicate sheets' compositions. The adsorption of PEG and dimethyldidecylammonium ions to the clay's alumina-silicate platelets increases the carbon, hydrogen, and nitrogen content. XPS photoelectrons have limited penetration depth and are very sensitive to adsorbed surface species. After modification, part of this depth consists of PEG and the quaternary ammonium species adsorbed on the surface and intercalated between the outer platelet layers. The XPS measured an increase in C and N atomic percentages (C from 39.3 to 54.6% and N from 2.4 to 3.7%) after PEG modification, confirming that dimethyldidecylammonium bromide exchange had increased the amount of alkylammonium ions over those present in the as-received PGW. The presence of Br 3p and $3d_{5/2}$ peaks at 67.75 and 68.68 eV (0.6 atomic percent) indicates that adsorption of some residual bromide into the surface regions from the quaternary ammonium salt ion exchange had also occurred.

Al and Si XPS edges in the as-received PGW clay appear, respectively, at 74.84 and 102.96 eV versus 74.3 and 102.43 eV for the PEG-modified PGW. These assignments were based on the peaks at 74.58 and 102.8 eV reported for Al and Si in Al_2SiO_4, respectively.[37,38] The as-received PGW exhibited one carbon 1s peak at 284.5 eV due to C present in the long alkyl chains of the ammonium pillars (e.g., $-CH_2$).[39a] This was used as the reference binding energy for the XPS spectra (Figure 2a). In comparison, two C 1s peaks were observed in PEG-modified PGW clay after deconvolution

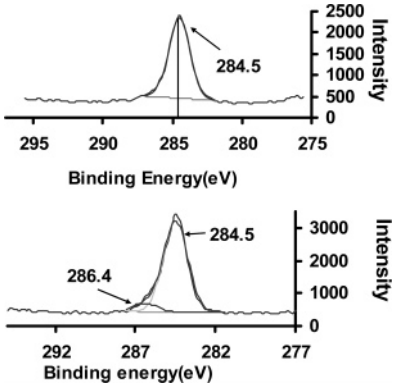

Figure 2. High-resolution C 1s XPS spectra of (a) as-received PGW and (b) PEG-modified PGW clay.

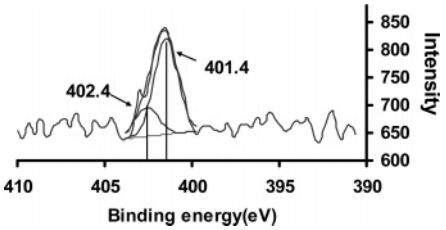

Figure 3. High-resolution N 1s XPS spectra of PEG-modified PGW clay.

(Figure 2b). The first, at 284.5 eV, is attributed to C in ($-CH_2-$) groups in the exchanged alkylammonium ions and the second, at 286.4 eV, indicates the presence of the ether-type O−C and of polyethyleneglycol.[39a,b] The nitrogen peak of as-received and PEG-modified PGW appears at a binding energy of 401.8 and 401.4 eV, respectively, in high-resolution spectra (Figure 3). We attribute this peak to nitrogen in the exchanged primary ammonium ions, which were originally present in the as-received PGW. This assignment is based on the 401.8 eV binding energy reported for N in ammonium ions (ammonium nitrate, ammonia trifluoroborate).[40,41] Deconvolution of the PEG-modified spectra reveals the presence of a second peak at 402.4 eV (Figure 3). Quaternary nitrogen from dimethyldidecylammonium ions should exhibit a peak near this energy, as suggested by the fact that the N 1s peak for tetrabutylammonium hydrogen sulfate has been reported at 402.2 eV.[42]

SAXS. SAXS studies were performed on all clay powders and all clay/polyDCPD composites. SAXS plots for I-28, I-44pa, and PEG-modified PGW clays are shown in Figure 4 and plots for nanocomposites formed from each of these clays are shown in Figures 5−7, respectively. The powdered clays (Figure 4a, b) exhibited d-spacings of 2.25 nm (I-28) and 3.2 nm (I-44pa and PEG-modified PGW). As-received PGW had a d-spacing of 2.31 nm (Figure 4b). The intensity of the main SAXS peak for PEG-modified PGW was much higher than that of I-44pa (Figure 4a), indicating PEG-modified PGW had a more highly ordered structure with the same average repeating platelet spacing as I-44pa. Further, a secondary peak was observed for both I-44pa and PEG-modified PGW at a q value of 0.395 Å^{-1}. This could be a secondary reflection of the first peak or a reflection from a small population of clays with d-spacings of 15 Å. It should be noted that an ∼15 Å mean d-spacing was observed by HR-TEM for dispersed PEG-modified PGW within the polyDCPD matrix, suggesting that the second reason is most likely.

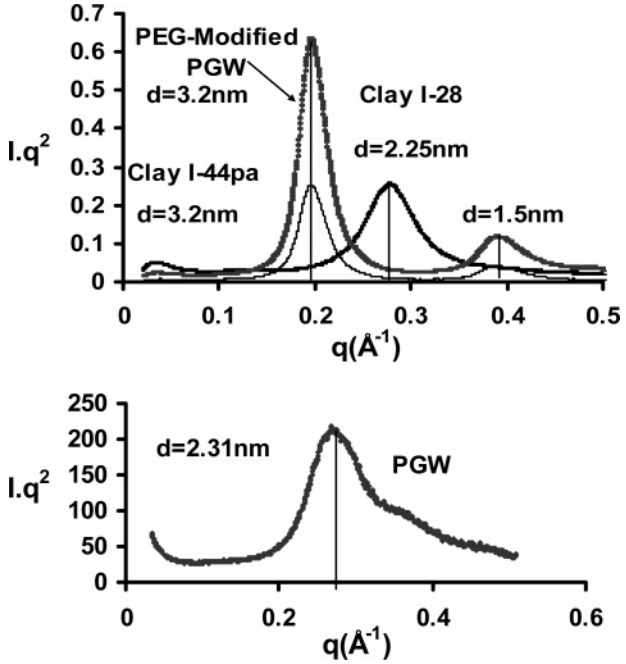

Figure 4. SAXS experiments on clay I-28, I-44pa, PGW, and PEG-modified PGW clay powders exhibiting d-spacings of 2.25, 3.2, 2.31, and 3.2 nm, respectively. (a) Lorentz-corrected SAXS plots of clay I-28 (d = 2.25 nm), I-44pa (d = 3.2 nm), and PEG-modified PGW(d = 3.2 nm) clay powders. (b) Lorentz-corrected SAXS plot of as-received PGW, d = 2.31 nm.

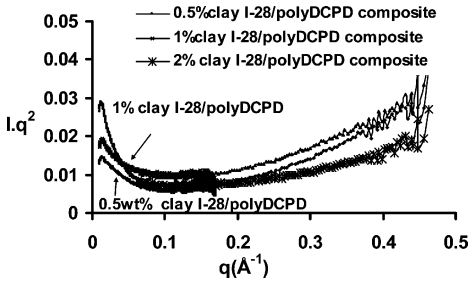

Figure 5. Lorentz-corrected SAXS plots of 0.5−2.0 wt% I-28 clay/polyDCPD composites.

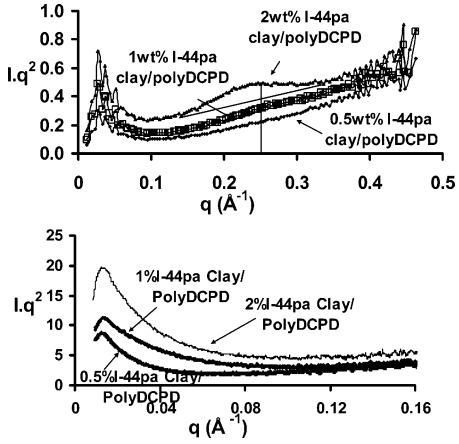

Figure 6. Lorentz-corrected small-angle X-ray scattering from I-44pa clay/polyDCPD composites containing 0.5, 1.0, and 2.0 wt% I-44pa clay. (a) q range from 0.04 to 0.4 Å^{-1}, 20 wt% 1-44pa clay/ployDCPD composite showed a peak at q = 0.253 Å^{-1}, $d = 2p/q$ = 24.8 Å (2.48 nm). (b) q range from 0.017 to 0.16 Å^{-1}.

The 0.5, 1.0, and 2.0 wt% I-28 clay/polyDCPD composites did not show any SAXS peaks within the q range of 0.017−0.4 Å^{-1} corresponding to d-spacings of 15.7−

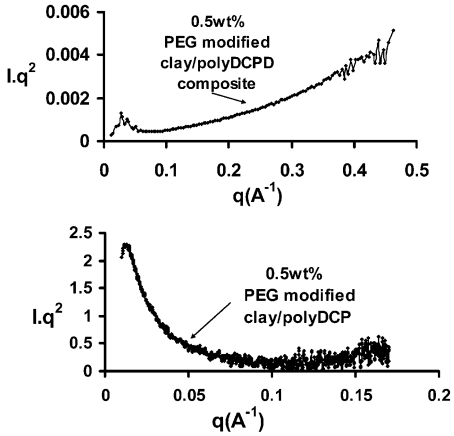

Figure 7. Lorentz-corrected small-angle X-ray scattering from the 0.5 wt% PEG-modified PGW clay/polyDCPD composite. (a) q range from 0.04 to 0.4 Å^{-1}; no peak was observed. (b) q range of 0.017 to 0.16 Å^{-1}; no peak observed.

369 Å (Figure 5). This suggests that a high degree of nanometer-scale dispersion was achieved in all of these composites after sonicating the clay in liquid DCPD for 3 h. This is consistent with previous XRD and TEM studies of these composites, which showed that partial exfoliation had produced dispersions of individual platelets and a variety of small tactoids within the resin.[11] The lack of Bragg scattering, as expected from repeated structures of equal spacings, suggests that a range of basal layer spacings are present within these small tactoids. In fact, the original I-28 ion-exchanged clay particles exhibited a range of d-spacings centered around 2.25 nm in the SAXS plot and 2.56 nm by XRD. Variable layer spacings can result from several mechanisms: (1) incomplete quaternary ammonium ion exchange with cations present in the as-received clay interlayers, (2) DCPD infusion within some interlayers, (3) variable total Fe or Fe^{3+}/Fe^{2+} composition within a tactoid which affects clay surface charge, and (4) small tactoid effects, in particular frayed platelets near edges of tactoids. Variation in persistence lengths (as observed by HR-TEM) could also result from any of the four factors listed above, as well as other reasons. Persistence lengths correspond to regions that have a constant value in the d-spacing over several adjacent layers within an individual tactoid.

SAXS plots of the 0.5 wt% I-44pa clay/polyDCPD composite did not show any peaks within the range $0.017 \le q \le 0.4$ Å^{-1} (Figure 6). The 1.0 wt% I-44pa clay/polyDCPD exhibited a very shallow peak, while the 2.0 wt% composite exhibited a broad peak in the range $0.142 \le q \le 0.34$ Å^{-1}, corresponding to d-spacings from 1.85 to 4.42 nm (Figure 6a). The maximum channel of this broad peak occurred at $q = 0.253$ Å^{-1}, corresponding to an interplatelet d-spacing of 2.48 nm. Thus, in addition to individual exfoliated clay platelets, tactoids are present with a distribution of d-spacings. SAXS plots of I-44pa clay/polyDCPD samples (0.5, 1.0, and 2.0 wt% clay) over the range $0.017 \le q \le 0.16$ Å^{-1} (corresponding to d-spacing from 3.92 to 36.9 nm) did not show any peaks (Figure 6b). Finally, no reflections were observed from the 0.5 wt% PEG-modified PGW clay/polyDCPD composite in either of the q ranges examined (Figure 7 a, b). Thus, no ordering could be observed after only 10 min of sonication of this clay in DCPD followed by curing.

SANS. SANS studies were performed on all the composite samples. There was no coherent scattering observed from the polyDCPD matrix; however, a relatively high incoherent background was present because the polyDCPD matrixes were not deuterated. The incoherent scattering background from a pure sample of polyDCPD (average of 0.75 cm^{-1}) was subtracted from the scattering obtained from composite samples. The difference represented scattering from dispersed clay particles. No peaks were observed in any of the plots of intensity versus q, or Iq^2 versus q. The SANS data were fit to the stacked-disk model developed by Glinka,[19a] Hanley et al.,[20,21] and Ho et al.[17,22] Clay platelets are assumed to be thin disk and tactoids to be a stack of thin disks[17] in this model for interpreting SANS data.[43−45]

Neutron scattering intensity is generally written as

$$I(q) = A\phi V_p(\rho - \rho_m)2P(q)S(q) \quad (1)$$

where A is an instrument constant, V_p is the volume of the particles, V is the total volume, $\phi = NV_p/V$ is the particle volume with N representing the number of particles, $\rho - \rho_m$ is the difference between the scattering length density of the particle and the polymer medium (contrast factor), $P(q)$ is the form factor and $S(q)$ is the structural factor.[19] $P(q)$ is the part of the scattering function influenced by the shape of the particle (in this case clay tactoid), and $S(q)$ is a measure of the interaction between the layers in a tactoid (short-range effects) and interaction between particles (tactoids), (long-range effects). The shape of clay platelets has been assumed to be thin disks to facilitate calculations.[43−45] For instance, the Glinka,[19a] Hanley et al.,[20,21] and Ho et al.[17,22] stacked-disk model treats clay platelets as thin disks and tactoids as parallel stacks of thin disks. The stacked-disk model is applied for the analysis of the experimental SANS data as described below. The form factor for a cylinder of radius R and height of $2H$ is

$$P(q) = 4\int_0^{\pi/2}\left(\frac{\sin^2(qH\cos\beta)}{(qH)^2\cos^2\beta}\right)\frac{J_1^{\,2}(qR\sin\beta)}{(qR)^2\sin^2\beta}\sin\beta d\beta \quad (2)$$

where J_1 is the first-order Bessel function, β is the angle between the wave vector, q, and major axis of the cylinder. The cylinder height, $2H$, represents a platelet thickness and can be defined as described below. In the limit of a very thin cylinder (i.e., a thin disk), $qH \ll 1$, the above equation simplifies to the Kratky−Porod expression:[46,47]

$$P(q) = \frac{2}{(qR)^2}\left[1 - \frac{J_1(2qR)}{qR}\right] \quad (3)$$

At the limit of very small q values ($q \to 0$), $P(q) = \exp(-q^2R^2/6)$.[20] This is an example of Guinier's law that states the slope should obey a power law with a slope of −2 for a very thin disk. The original Guinier's law to obtain the radius of gyration for any random shape of particles or the modified Guinier's law to obtain the radius of disks implies the scattering is a power-law scattering.

The form factor for an organically modified clay with core thickness of $2H$ and surfactant layer thickness of d is denoted as $P_{s,c}(q)$. The form factors of the core platelet (P_c (q)), the core plus exchanged alkylammonium layer ($P_s(q)$), and total ($P_{s,c}(q)$) are defined, respectively, as[17,21,22]

$$P_c(q) = \int_0^{\pi/2}\left[\left(\frac{\sin(qH\cos\beta)}{qH\cos\beta}\right)\times \left(\frac{2J_1(qR\sin\beta)}{qR\sin\beta}\right)\right]^2 \sin\beta d\beta \quad (4)$$

$$P_s(q) = \int_0^{\pi/2}\left[\left(\frac{\sin(q(d+H)\cos\beta)}{q(d+H)\cos\beta}\right)\times \left(\frac{2J_1(qR\sin\beta)}{qR\sin\beta}\right)\right]^2 \sin\beta d\beta \quad (5)$$

$$P_{c,s}(q) = \int_0^{\pi/2}\left[\left(\frac{\sin(q(d+H)\cos\beta)}{q(d+H)\cos\beta}\right)\times \left(\frac{\sin(qH\cos\beta)}{qH\cos\beta}\right)\left(\frac{2J_1(qR\sin\beta)}{qR\sin\beta}\right)\right]^2 \sin\beta d\beta \quad (6)$$

Clays occur as ordered stacked layer structures (tactoids) with individual platelets bonded together by ionic attractions between negatively charged clay platelets and cations. For low clay loadings, interactions between well-separated tactoids (i.e., individual stacked disks) are negligible and the scattering response is influenced predominantly by the short-range structural factor, $S_s(q)$, that describes scattering within an individual tactoid. In that case, long-range contributions to the scattering response can be neglected, i.e., $S(q) \approx S_s(q)$. According to eq 1, the scattering intensity, $I(q)$, depends on the product of $P(q)S(q)$. $P(q)$ is the square of the scattered wave amplitude averaged over all directions $\langle f^2\rangle$ (the platelet core, $f^2_c(q)$, the ammonium coated platelet, $f^2_t(q)$, and the interaction term, $f_c(q)f_s(q)$). Therefore, $S_s(q)$ should be multiplied by $f^2_c(q)$, $f^2_s(q)$, $f_c(q)f_s(q)$ given in eqs 4−6.[17,21,22] If the nearest neighbor-to-neighbor distances in a stack of clay platelets obeys a Gaussian distribution, the short-range structural factor can be written[17,46]

$$S_s(q) = 1 + \frac{2}{N}\sum_{k=1}^{N}(N-k)\cos(kDq\cos\beta)\times \exp[-k(q\cos\beta)^2\sigma^2/2] \quad (7)$$

where N is the number of platelets in a stack, D is the nearest neighbor-center-to-center distances, and σ is its Gaussian standard distribution (GSD), respectively. Therefore, the total coherent scattering intensity of randomly oriented stacks of clay platelets (from eq 1) assuming a dilute dispersion of tactoids, i.e., $S(q) = S_s(q)$, can be written as[17]

$$I^{\mathrm{OMMT}}_{\mathrm{total}}(q) = N\int_0^{\pi/2}[\Delta\rho_1(V_t f_t(q) - V_o f_c(q)) + \Delta\rho_c V_o f_c(q)]^2 S_s(q)\sin\beta d\beta \quad (8)$$

where N is the number of clay platelets in a stack, $\Delta\rho_1$ is the scattering length density difference between core (e.g., the clay platelet's alumina silicate layer) and medium (polyDCPD), $\Delta\rho_c$ is the scattering length *density* difference between the alkylammonium ion layer and the medium (polyDCPD), V_t is the total volume of the alumina silicate core and alkylammonium ion layer, and V_c is the volume of the core.[17] The wave amplitudes, f_c and $f_{c,s}$, are derived from eqs 4−6 via the relations $P_c(q) = \langle f_c^2(q)\rangle$ and $P_{c,s}(q) = \langle f_c(q)f_s(q)\rangle$, which are averages over all directions of the wave amplitudes. The structural factor for a dilute dispersion of tactoids is given by eq 7. When all platelets have been completely separated from the stacks and dispersed as individual platelets (e.g., fully exfoliated, $N = 1$), eq 7 yields $S_s(q) = 1$, and eq 8 simplifies to eq 9. Only short-range structural factors are important for very low concentrations. However, interactions between stacks become increasingly important with higher clay loading, and in that case, long-range structural factors should then be calculated.

$$I^{\mathrm{OrganicModified}}_{\mathrm{Single}}(q) = N_{OMMT}\int_0^{\pi/2}[\Delta\rho_1(V_t f_t(q) - V_o f_c(q)) + \Delta\rho_c V_o f_c(q)]^2 \sin\beta d\beta \quad (9)$$

The incoherent background was subtracted from the scattering intensity for each sample. The slopes of $I(q)$ versus q for the 0.5, 1.0, and 2.0 wt% I-28 clay/composites varied between −2.53 and −2.79 over the range $0.003 \le q \le 0.05$ Å^{-1} (Figure 8). The $I(q)$ vs q slopes for 0.5,1.0, and 2.0 wt% I-44pa clay/polyDCPD nanocomposites varied from −2.5 to −2.76 over the range $0.003 \le q \le 0.06$ Å^{-1} (Figure 9). A slope of −2.57 was found for the 0.5 wt% PEG modified clay/polyDCPD composite within the range $0.003 \le q \le 0.05$ Å^{-1} (Figure 10). A slope of ~ -2 indicates the presence of noninteracting thin disks, while a slope of −3 is given by fractal shapes.[31b] The experimental slopes larger than −2 indicate the presence of platelets and tactoids of various thicknesses, which are bent and curved (fractal contribution to shape). The plots of scattering intensity vs wave vector within the range $0.003 \le q \le 0.05$ Å^{-1} were fitted to the stacked-disk model for each of the composites. The scattering length densities of the alumina silicate core, alkylammonium ion layer, and polyDCPD were known (Table 1), as were the clay volume fraction and the clay layer d-spacings (from SAXS and HR-TEM analysis). These values were used as input to the stacked-disk model from which the mean number of clay platelets per tactoid was predicted for each composite. The results are summarized in Table 2.USANS data showed linear plots with the same slopes that were present in the SANS region for all of 0.5, 1.0, and 2.0 wt% I-28 clay/polyDCPD and 0.5, 1.0, and 2.0 wt% I-44pa clay polyDCPD composites (Figures 8a and 9a). No Guinier regions were observed in any of these composites. The absence of a Guinier region indicates that interactions between particles exist.[23,32d] The USANS data for 0.5 wt% PEG-modified PGW clay composite was not available due to multiple scattering effects.

The fitting parameters for 0.5 wt% I-28 clay/polyDCPD and 0.5 wt% I-44pa/polyDCPD composites are presented in Table 2. Figure 11 shows the agreement between the model and the 0.5 wt% I-28 composite experimental data using the fitting parameters presented in the Table 2. The q range of $2.5 \times 10^{-3} < q < 0.1$ Å^{-1} was used for fitting. The intensity data in the q range larger than 0.1 were not used because the noise associated with these data, after subtracting the background, may not be reliable. The d-spacings used for fitting are from the original d-spacings of the clays obtained from SAXS experiments.

HR-TEM. A limitation of TEM and HR-TEM studies, in comparison to scattering techniques, is that the region analyzed is relatively small (square micrometer area multiplied by thickness of thin section), as opposed to neutron and X-ray scattering measurements, which

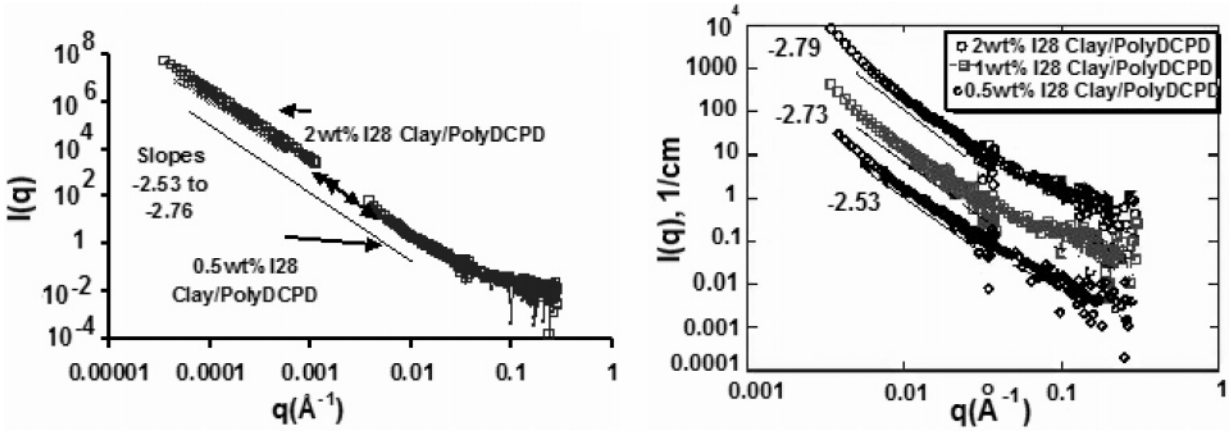

Figure 8. Small angle neutron scattering (SANS) and ultrahigh-resolution small-angle neutron scattering (USANS) of 0.5−2.0 wt% I-28 clay/polyDCPD composites. (a) SANS and USANS of 0.5 and 2.6 wt% I-28 clay/polyDCPD composites. (b) SANS from scattering from 0.5, 1.0, and 2.0 wt%polyDCPD composites. The slopes of $I(q)$ vs q are between −2.53 and 2.79 for $q < 0.05$.

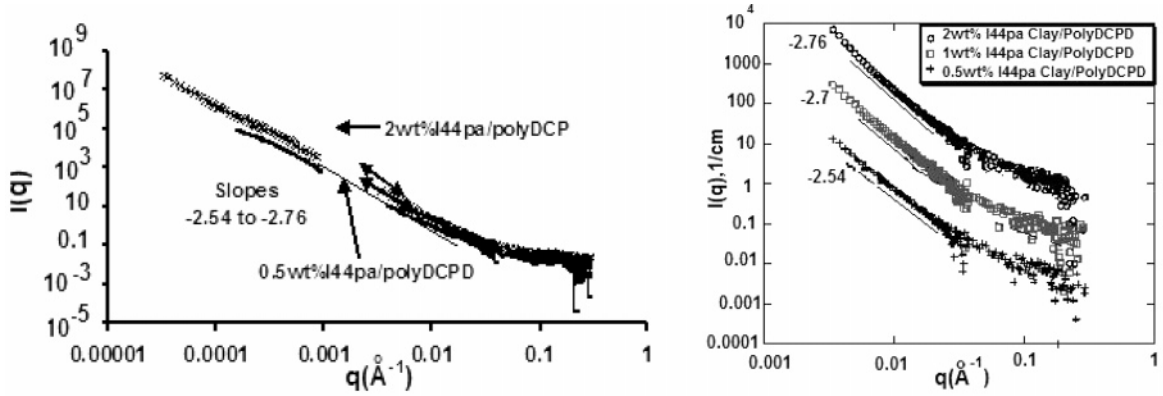

Figure 9. Small-angle neutron scattering (SANS) and ultrahigh-resolution small-angle neutron scattering (USANS) of 0.5−2.0 wt% I-44pa clay/polyDCPD composites. (a) SANS and USANS of 0.5 and 2.6 wt% and I44pa/polyDCPD composites. (b) SANS from 0.5, 1.0, and I44pa/polyDCPD composites. The slopes of $I(q)$ vs q are between −2.54 and −2,76 for $q < 0.06$.

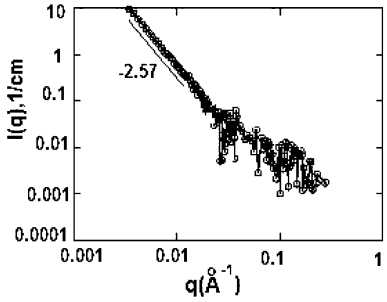

Figure 10. Small-angle neutron scattering from the 0.5 wt% PEG-modified PGW clay/polyDCPD composite. The slope is −2.57 for $q < 0.05$.

sample cubic-centimeter volumes. To provide a more representative characterization of the specimen, as a whole, many regions of the nanocomposites were examined by TEM and HR-TEM. Examination by TEM demonstrated that high degrees of clay delamination were achieved within the polyDCPD matrix for all three types of clay at 0.5 wt% (Figure 12). To quantify the degree of delamination, two parameters were measured: the mean number of individual clay platelets per tactoid (tactoid size) and the distribution of (001) basal layer spacings (d-spacing) for all tactoids. Tactoid size distributions were also measured providing the range of tactoid sizes (platelets per tactoid) present. The results of these measurements are discussed below. They are used to test, for the first time, the application of the stacked-disk model to interpret SANS experiments on nanodispersed clays.

A range of microstructure was exhibited in the three nanocomposite series of clay dispersions. The sizes of the dispersed tactoids varied. The smallest mean tactoid sizes were seen in the 0.5 wt% I-28 clay/polyDCPD composite, while the largest mean tactoid sizes for the 0.5 wt% series were observed in the 0.5 wt% PEG-modified clay/polyDCPD composite (see Table 3). Representative examples of tactoids in these I-28, I-44pa, and PEG-modified PGW clay/polyDCPD composites are shown in Figures 13, 14, and 15, respectively. On the sides of these figures, magnified micrographs are shown (5 nm scale bars) with arrows pointing to the locations in the central portion (20 nm scale bars) from which these expanded views were taken. In Figure 13a, a tactoid is shown containing eight platelets from the 0.5 wt% I-28 sample. It has been splayed into two sections at the end, each section consisting of four platelets. Tactoids with thicknesses of 3−5 nm, along with several single platelets, and two-platelet tactoids are displayed in Figure 13b from the 2.0 wt% I-28 sample. Some diffusion of polyDCPD (intercalation) appears to occur within the center of the tactoid displayed in the upper left corner. In comparison, the mean sizes of the tactoids in 0.5 wt% PEG-modified PGW and the 0.5 and 2.0 wt% I-44pa composites were somewhat larger than those in the corresponding wt% I-28 samples (e.g., see Figure 14, Figure 15 and Table 3). In Figure 14a, two tactoids with nine and five platelets are shown. Several indi-

Table 1. Physical Properties of Materials

material	molecular mass (g)	density (g/cm^3)	neutron scattering length density[a] (SLD) (Å^{-2})
poly(dicyclopentadiene) $(C_{10}H_{12})_n$	$(132.2)_n$	1.1	1.08×10^{-6}
dimethyldidecylammonium ion	326.62	0.9	-4.61×10^{-7}
trimethyloctadecylammonium ion	312.6	0.9	-3.97×10^{-7}

[a] Calculated from the formula: SLD = $\sum b_{ci}/v_m$, where b_{ci} is the bound coherent scattering length of ith of n atoms in a molecule with molecular volume v_m.[47] SLD's were calculated using NIST's web calculator (http://www.ncnr.nist.gov/resources/sldcalc.html).

Table 2. Example Fitting Parameters Used for Fitting the Stacked-Disk Model to the Experimental Data of the 0.5 wt% I-28 Clay/ and 0.5 wt% I-44Pa Clay/PolyDCPD Composites

composite	volume fraction	disk radius Å	alumina silicate core thickness Å	surfactant layer thickness Å	alumina silicate core SLD Å^{-2}	surfactant layer SLD[a] Å^{-2}	polyDCPD SLD Å^{-2}	number of platelets in stack[b]
0.5 wt% I-28/polyDCPD	0.002233	5000	10	12.5	4×10^{-6}	-3.97×10^{-7}	1.08×10^{-6}	4
0.5 wt% I-44pa/polyDCPD	0.002233	5000	10	22	4×10^{-6}	-4.61×10^{-7}	1.08×10^{-6}	4

[a] Note that the surfactant SLD varies with the pillaring agent used and the average number of platelets/stack from the best fit to the data.[b] [b] This is the best value for fitting the predicted I vs q from the stacked-disk model to the experimental I vs q data.

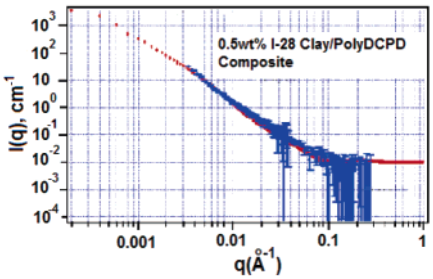

Figure 11. Fitting the stacked-disk-model prediction (blue) using the parameters in Table 2 versus the SANS experimental data (red) of 0.5 wt% I-28 clay/polyDCPD composite in the q range of $2.5 \times 10^{-3} < q < 0.1$ Å^{-1}.

vidual platelets and two-platelet tactoids are present in close proximity with the larger tactoids. In Figure 15, one 20−25 nm tactoid splits at a branch point into two smaller tactoids. It appears that the polyDCPD texture extended directly between these tactoid branches and interfaces directly with the tactoid surface. Good surface wetting of the clay platelets tactoids was observed for all composites, and no voids were observed.

The distributions of tactoid sizes (platelets per tactoid) for polyDCPD composites with 0.5 and 2.0 wt% I-28 clay, 0.5 and 2.0 wt% I-44pa clay, and 0.5 wt% PEG-modified PGW clay were measured from a large number of HR-TEM micrographs. The results are shown in Figure 16 and summarized in Table 3. The mean number of platelets per tactoid for 0.5 wt% I-28 was 3.2 (median = 1.9) on the basis of the examination of 250 different tactoids (Figure 16a). The largest tactoid observed in this sample had only 12 platelets. There was a significant population of single clay platelets dispersed in this sample. The mean tactoid size for the 0.5 wt% I-44pa composites was 4.2 platelets (median = 2.8) on the basis of 447 tactoids (Figure 16c). However, the largest tactoid observed had 26 platelets, approximately twice as large as that in the 0.5 wt% I-28 clay/polyDCPD composite (Figure 16b). Upon increasing the I-28 clay concentration to 2.0 wt%, the mean tactoid size increased to 3.3 platelets (median = 2.3) on the basis of 309 tactoids. The largest tactoid observed for the 2.0 wt% I-28 sample, however, had 65 platelets, much larger than the 12 platelets observed in the 0.5 wt% I-28 sample. The 2.0 wt% I-44pa composite (Figure 16b) exhibited a mean tactoid size of 6.2 platelets (median = 5.2) on the

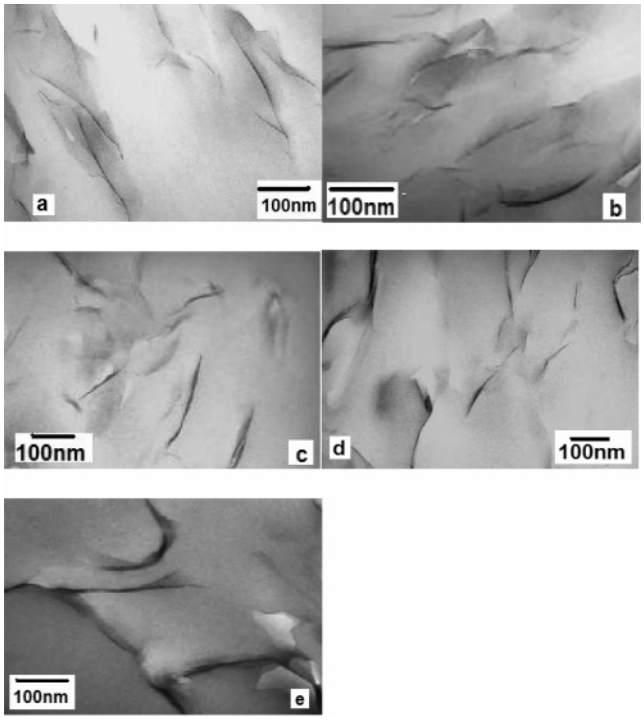

Figure 12. (a−e) TEM micrographs of nanodispersed clay in polyDCPD composites. Samples (a−d) sonicated for 3 h, and sample e sonicated for 10 min. (a) 0.5 wt% I-28 clay, (b) 2.0 wt% I-28 clay (c) 0.5 wt% I-44pa, (d) 2.0 wt% I-44pa clay, and (e) 0.5 wt% PEG-modified PGW clay.

basis of examinations of 454 tactoids. The largest tactoid found had 102 platelets.

The 0.5 wt% PEG-modified PGW clay/polyDCPD composite was prepared by sonicating the clay in DCPD for only 10 min prior to curing in comparison to 3 h of sonication for the I-28 or I-44pa samples. The mean tactoid size in this composite was 6.2 platelets (median = 4.9), and the largest observed tactoid had 23 platelets on the basis of 198 tactoids studied. Although the distribution of tactoid sizes for the 0.5 wt% PEG-modified PGW was shifted to somewhat larger sizes than either the 0.5 wt% I-28 or I-44pa compositions, the 18-fold smaller sonication time used with this clay indicated that PEG-modified PGW clay delaminated more rapidly than the I-28 and I-44pa clays.

Table 3. Comparison of the Mean Tactoid Sizes Predicted from SANS Data Using the Stacked-disk Model with Those Measured Directly by HR-TEM

	composite sample						
	I-44pa clay/poly(DCPD)			I-28 clay/poly(DCPD)			PEG-modified clay/polyDCPD
wt% clay	0.5	1	2	0.5	1	2	0.5
Predicted by Stacked-Disk Model (SANS data)							
mean (GSD)[a]	4	5	14	4	7	11	5
Observed by HR-TEM							
median	2.8		3.2	1.9		2.3	4.9
mean	4.2		6.2	3.2		3.3	6.2
tactoid size range (no. of platelets)	1−26		1−102	1−12		1−65	1−23
number of tactoids examined	447		454	250		309	198

[a] Gaussian Standard Distribution.

The most common tactoid size in all composites was two platelets. At least 30% of the tactoids had two platelets in the 0.5 and 2.0 wt% I-28 clay/polyDCPD and 0.5 and 2.0 wt% I-44pa/polyDCPD composites. In the 0.5 wt% PEG-modified PGW composite, 19% of the tactoids contained two platelets.

HR-TEM *d*-spacings. The layer spacing (*d*-spacing) between platelets in tactoids was also measured from HR-TEM micrographs for the clay/polyDCPD composites containing 0.5 and 2.0 wt% I-28, 0.5 and 2.0 wt% I-44pa, and 0.5 wt% PEG-modified PGW (Figure 17). The relative populations of basal layer spacings for each specimen (filled squares) are plotted as accumulative percentages on the ordinate in logarithmic scale, and each was linear-least-squares fit to a log-normal distribution, d*f*/d ln(*x*). The error for an individual (001) layer spacing measurement was ±0.15 Å (placed at the right along the ordinate for visual comparison).

Of the three series of clay dispersions, the 0.5 wt% PEG-modified PGW clay/composite exhibited the largest mean *d*-spacing of 15.5 Å (and a log-normal fitted median of 15.4 Å). The mean [and log-normal fitted median] *d*-spacings for the other examined nanocomposites were 13.4 [13.3] (0.5 wt% I-28), 12.2 [12.1] (2.0 wt% I-28), 13.6 [13.4] (0.5 wt% I-44pa), and 13.7Å [13.6 Å] (2.0 wt% I-44pa), respectively. The distributions of *d*-spacings are almost the same within the tactoids in the composites containing I-28 and I-44pa clays. Each of these composites was prepared from clay containing alkylammonium ion pillaring agents as the only organic modifier. The *d*-spacings are the largest for the PEG-modified PGW clay, presumably due to partial PEG intercalation between some platelets within the dispersed tactoids.

The mean clay *d*-spacings within the composites are much smaller than the *d*-spacings of the precursor modified clays used to prepare these composites. The starting clays had *d*-spacings of 22.5 (I-28) and 32 Å (I-44pa and PEG-modified PGW), as measured by SAXS. However, SAXS plots of the I-44pa and PEG-modified PGW clays exhibited a secondary peak corresponding to 15 Å *d*-spacings most likely arising from a small subpopulation of collapsed clays or alternatively to second-order reflection of ∼32 Å peak. Since second- and higher-order diffraction peaks can only be observed with rather perfect crystals, the imperfections in the tactoids work to smear or diminish the diffracted intensity contributions to these higher-order peaks. Therefore, following nanodispersion and DCPD curing, the sharp drop in the dominant *d*-spacing is almost certainly due to the presence of a large population of smaller *d*-spacings remaining.

The following mechanism appears to be responsible for the reduction in *d*-spacing. Sonication and mixing preferentially cleave tactoids along those platelets which were the most loosely bound, i.e., those separated by the largest spacing due to effective pillaring of alkylammonium ions exchanged into the clay used. If the original distribution of layer spacings in the pillared clay particles possessed a small population of platelet spacings in the 8 to ∼15 Å range (as suggested by the secondary SAXS peak in the treated clay), this population would preferentially survive delamination, as particles and larger tactoids were progressively split into smaller tactoids and individual exfoliated platelets. Platelets with smaller *d*-spacings are more strongly attracted to one another. Most likely, the original ion exchange of the ammonium ion pillaring agents into the clays did not result in complete ion exchange in all the interlayers. Those nonmodified interlayers (with small *d*-spacings) would be more difficult to cleave because they would contain cations that more strongly bound platelets together than those in the alkylammonium ion-modified interlayers. Thus, the fraction of originally unpillared platelet stacks would increase as cleavage occurs between pillared platelets, leaving small tactoids having mostly small *d*-spacings between platelets. It should be noted that alkylammonium ion pillars undergo Hoffman elimination reactions at ∼200 °C. Since a high temperature (above 200 °C) curing step was applied to the composites after thorough cross-linking had occurred at 160 °C,[11] a decrease in the mean *d*-spacings could result if the pillars between clay layers within the tactoids decompose and platelets close together.

Clay sheets are three-dimensional and can have a turbostratic morphology. Consequently, image contrast produced by basal layers in a given tactoid can vary due to differences in thickness and crystallographic orientation of the clay sheets with respect to the electron-beam direction. For example, bending of the clay sheets in a tactoid can orient a portion of each sheet away from the edge-on configuration, proportionally reducing fringe contrast from the respective sheets. Therefore, when individually counting the existing platelets present in the 1658 tactoids summarized in Table 3, it was important to clearly tally only the platelets and not confuse them with 'anomalous' fringes which may appear. The tactoids in this study rarely exhibited such anomalous fringes. When they appeared, they were easy to recognize and they were not counted.

The (001) basal layer spacings and the number of clay platelets per tactoid were measured between adjacent fringes that exhibited strong contrast over a straight length of at least ∼25 nm with no discernible/significant contrast features between the fringes. Since the spacing between adjacent fringes can vary along their length, three *equant*-spaced measurements were made along the selected high-contrast, straight segment of the pair of fringes, and these measurements were averaged together. On rare occasions, regions of tactoids exhibited very fine, additional fringes between the dominant broader fringes that were sensitive to the lens defocus. An example of this is clearly depicted in Figure 18. These 'anomalous' fringes are interpreted as either (a) arising from possible lattice contrast from curved clay

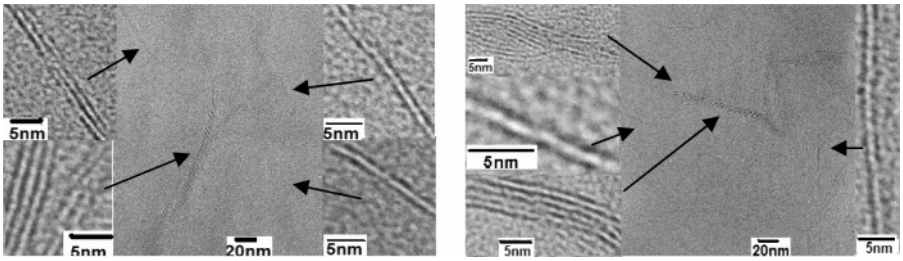

Figure 13. HR-TEM micrographs from I-28 clay/polyDCPD composites. (a) 0.5 wt% I-28. (b) 2.0 wt% I-28.

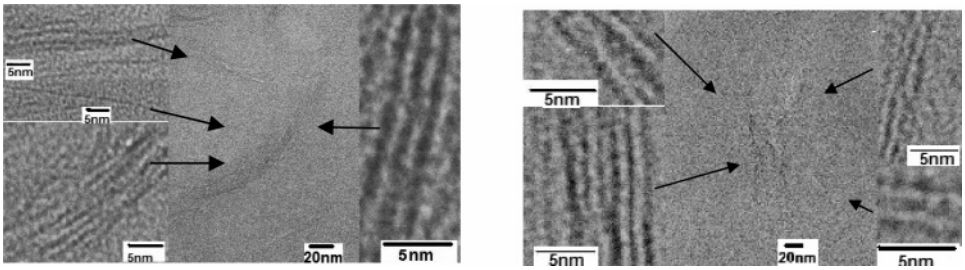

Figure 14. HR-TEM micrographs from I-44pa clay/polyDCPD composites. (a) 0.5 wt% I-44 pa. (b) 2.0 wt% I-44pa.

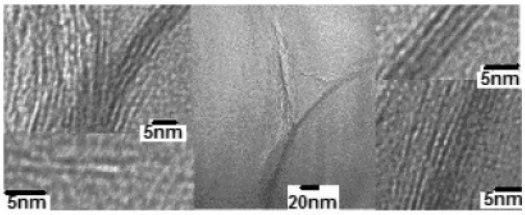

Figure 15. HR-TEM micrograph of the 0.5 wt% PEG-modified PGW clay/polyDCPD composite.

sheets whose sheet normal deviated from perpendicular to the electron-beam direction or (b) arising from a mineral impurity. In any event, the platelets in these anomalous regions were not counted as clay layers per tactoid and the layer spacings of 'anomalous' fringes were not measured.

Experimental Test of SANS Stacked-Disk Model. The model predictions for the mean number of platelets per tactoid based on the fitting of SANS experimental data (for the three series of nanocomposites) to the stacked-disk model are shown in Table 3 along with the mean and median values from HR-TEM analysis. Since HR-TEM sampled a large number of tactoids in each nanocomposite examined, the HR-TEM results are reasonably representative of the tactoid distribution within the whole sample. The SANS stacked-disk model predictions are in good agreement with direct HR-TEM measurements for all three of the 0.5 wt% clay nanocomposites (I-28, I-44pa, and PEG-modified PGW clay). However, as the clay loading in the composites increased, differences between the stacked-disk-model predictions and HR-TEM results become larger. The stacked-disk model treats clay tactoids as rigid, parallel-stacked thin disks. Although this may approximate the shape of very small clay tactoids, Montmorillonite clay tactoids have complex shapes that branch (e.g., see Figure 15) and are often curved (e.g., see Figure 12). The geometric complexity of the clay tactoids increases with tactoid size, greatly departing from the model treatment. Larger tactoids are far thicker than an individual platelet, but the length and width dimensions do not change as sharply. Thus, the distribution of tactoid surface to thickness (e.g., l × w/thickness) ratios broadens.

The slope of I versus q (log−log plots) in the stacked-disk model in the q range of $0.001 < q < 0.06$ Å for a thin disk is −2. As the thickness of the disks increases (stacked disk), at constant diameter, the absolute values of the slope increase. For example, as the ratio of the diameter to the thickness of the disk (aspect ratio) in the stacked disk model was decreased from 222.2 to 11.11, the calculated absolute values of slopes increased from 2.14 to 2.86. This corresponds to the change from a single platelet to a tactoid of 20 platelets, when using tactoids with a diameter of 5000 Å, a core thickness of 10 Å, and a pillaring agent or gallery of 12.5 Å.

Therefore, the absolute values of slopes observed in the SANS data are expected to be larger than 2. With an increase in the mean number of platelets per tactoids that occurs upon increasing the clay loadings, the absolute values of the slopes must deviate from 2 toward 3. However, the distribution of the tactoid sizes (Figure 16) is complex, and these distributions, as well as curvature and other geometrical factors, contribute to the slope. The deviation of the average number of platelets per tactoid (predicted by fitting SANS data to the stacked disk model) from the values observed by HR-TEM (Table 3) as clay loading increased is not surprising considering the distributions of tactoid sizes, thicknesses, and the turbostratic curvatures of the platelets and tactoids present in these composites.

It stands to reason that stacked-disk-model predictions of composites with large tactoid sizes would be questionable. In fact, in 2 wt% clay samples, the model predictions from SANS data do deviate significantly from direct HR-TEM measurements. Furthermore, the stacked-disk model does not take into consideration long-range structural factors, which could be increasingly important with greater clay loadings (higher clay volume fractions) where the interactions between different clay tactoids may become more significant. The absence of a Guinier region in the USANS data also suggests the particles could have interacted. However, the mean number of tactoids per unit area observed by TEM did not increase, but actually this value decreased with higher clay loading (Table 4). Instead, the mean tactoid thickness did increase. Thus, a strong argument for the increasing contribution of long-range structural factors cannot be made. Only short-range structural

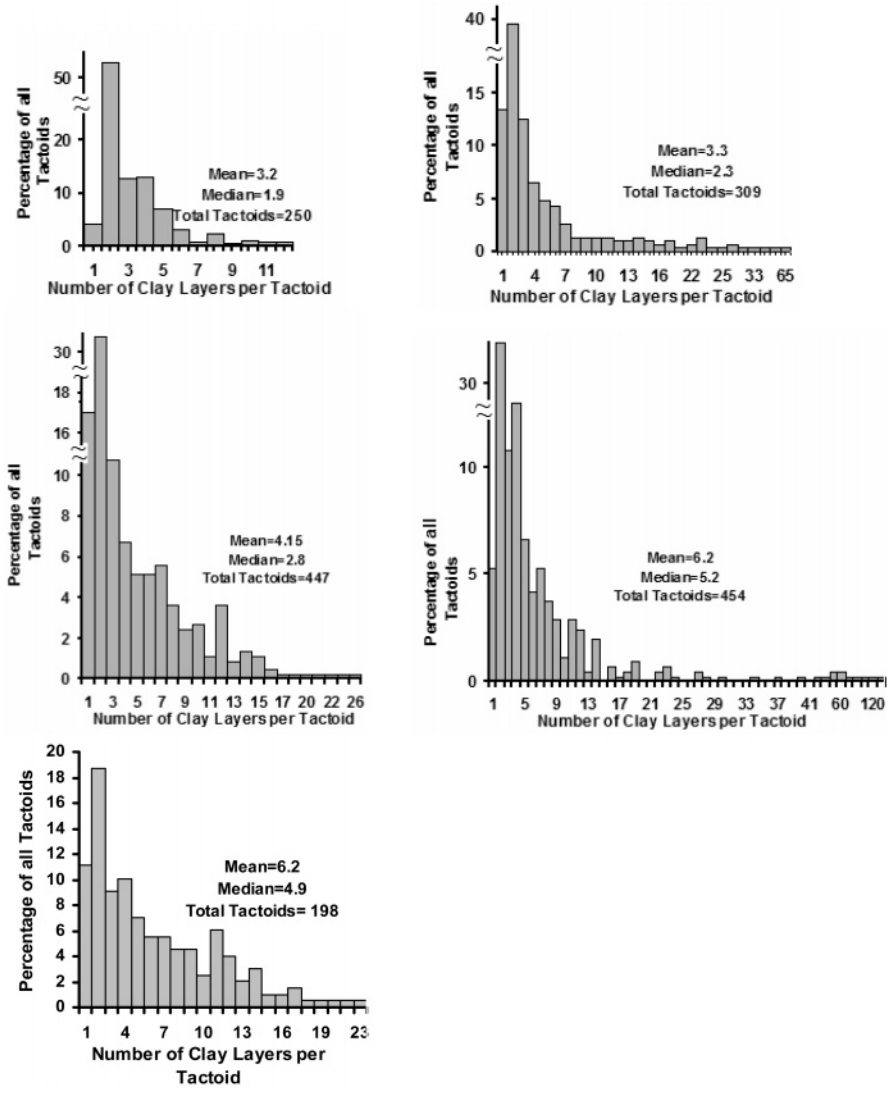

Figure 16. The distribution of tactoid sizes within the matrixes of clay/polyDCPD nanocomposites. Tactoid sizes are expressed as clay platelets per tactoid. (a) Distribution of tactoid sizes within the 0.50 wt% I-28 clay/polyDCPD composite. The mean was 3.2, and the median, 1.9, was platelets per tactoid. (b) Distribution of tactoid sizes within the 2.0 wt% I-28 clay/polyDCPD composite. The mean was 3.3, and the median was 2.3 platelets per tactoid. (c) Distribution of tactoid sizes within the 0.5 wt% I44 clay/polyDCPD composite. The mean was 4.2, and the median was 3.1 platelets per tactoid. (d) Distribution of tactoid sizes within the 2.0 wt% I44 clay/polyDCPD composite. The mean was 6.2, and the median was 5.2 platelets per tactoid. (e) Distribution of the tactoid sizes within the 0.5 wt% PEG-modified clay/polyDCPD nanocomposites. Tactoid sizes are expressed as clay platelets per tactoid.

factors originating from interactions between the stacked platelets in a tactoid are considered in the model. Furthermore, neither the exfoliated platelets nor the tactoids present are uniformly dispersed throughout the poly(DCPD) matrix. Some regions have more dispersed clay, and other regions contain less. The stacked-disk model assumes a uniform distribution, and this may account for the small discrepancies with the direct TEM results at low clay loadings. These factors may cause the stacked-disk model's predictions to deviate from the actual mean number of platelets per tactoid. The large number of tactoids sampled in each case by HR-TEM provides confidence that these results are reasonably representative of the tactoid distribution within the whole sample. This compensates for TEM's limitation as a local analytical technique.

Exfoliation in the Nanocomposites. As clay tactoids exfoliate and become smaller, the resistance to further exfoliation should increase. Exfoliation should become impeded by geometric constraints as delaminated platelets impinge on one another, blocking pathways for further separation. Furthermore, the viscosity of the liquid monomer/clay mixture increases during this process, slowing transport of exfoliated platelets away from their parent tactoids. Evidence supporting this picture is provided by HR-TEM characterizations of the nanocomposite microstructures. The mean number of tactoids (including individual clay platelets) per unit area was measured from many regions of each nanocomposite. If each nanodispersion process encountered no resistance, homogeneous dispersions would result and the density of tactoids (and platelets) would scale with clay loading. In the presence of dispersion resistance, the density of tactoids (and platelets) would be heterogeneous within any one nanocomposite while the process proceeded. Further, the density of tactoids (and platelets) for the same clay loading would vary with dispersion resistance. This all assumes equivalent processing during delamination (i.e., the same sonication times and energies as were applied in this study).

Table 4 summarizes the mean number of tactoids (including individual clay platelets) per unit area for

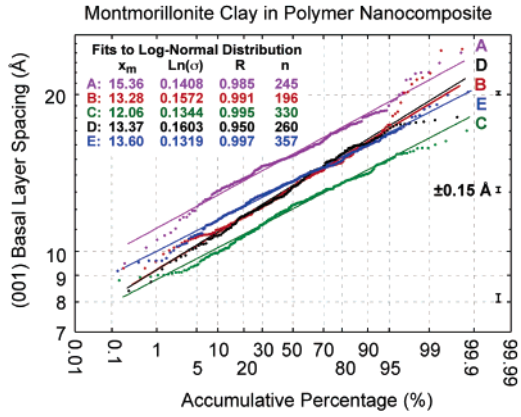

Figure 17. Distribution of (001) layer spacings (d-spacing) of the clay tactoids dispersed in poly(DCPD) nanocomposites. (A) PEG-modified PGW clay (0.5 wt%) (B) I-28 clay (0.5 wt%), (C) I-28 clay (2.0 wt%), (D) I-44pa clay (0.5 wt%), and (E) I-44pa (2.0 wt%). Several error bars representing the precision of the individual measurements are placed at the right along the ordinate for visual comparison. The median (x_m) and width (σ)) of the distribution were used as the fitting parameters from which the corresponding mode (x_o) and mean of the distribution can be derived.

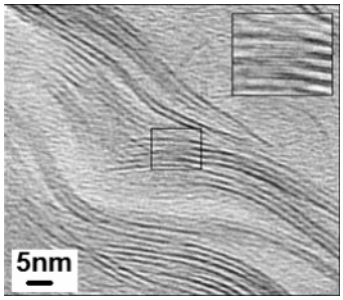

Figure 18. Defocusing anomalies in a tactoid within the 2 wt% I44pa/polyDCPD composite which were not be counted in the measurements of either d-spacings or the number of clay platelets per tactoid.

each composite and the total surface area examined (HR-TEM). The 0.5 wt% I-28 composite had the largest number of tactoids (and platelets) per unit area, 2.21×10^8 per mm^2. The 2.0 wt% I-28 composite had 1.91×10^8 tactoids (and platelets) per mm^2. Thus, as clay loading increased, the degree of exfoliation and nanodispersion decreased when sonication time was held constant. The same trend was observed for I-44pa clay composites. The 0.5 wt% I-44pa composite exhibited 2.05×10^8 tactoids (and platelets) per mm^2, while the 2.0 wt% analogue had 1.99×10^8 per mm^2. Increasing the clay loadings did not increase the number of clay fragments formed. Therefore, the samples with 2.0 wt% loading experienced a higher dispersion resistance than those with 0.5 wt% loading, so the mean tactoid size did not decrease as much. During sonication, the same amount of energy was applied to each sample. Consequently, less energy was received per clay particle for the higher loadings and, therefore, less cavitation at those clay surfaces. Among the 0.5 wt% loadings, the PEG-modified PGW nanocomposite exhibited the smallest density of tactoids (and platelets), by about 1 order of magnitude, because this composite was sonicated for only 10 min prior to curing (e.g., 1/18th the energy input to the other samples). Measurements of the tactoid size (mean number of platelets per tactoid, see Table 3) are consistent with the inferred dispersion resistances on the basis of the measured density of tactoids (and platelets) (Table 4). In particular, tactoid sizes increased with higher clay loadings, indicating less delamination occurred. The clay that exhibited the smallest density of tactoids (and platelets), PEG-modified PGW, also exhibited the largest tactoid sizes.

Conclusions

PolyDCPD/clay nanocomposites were synthesized by delaminating chemically modified Montmorillonite clays (Nanomer: I-28, I-44pa and PEG-modified PGW) in the monomer DCPD, followed by curing. The clays were nanodispersed in low-viscosity liquid DCPD by stirring and sonication prior to curing. After dispersion, solid samples were prepared by ring-opening metathesis polymerization. A combination of SAXS, SANS/USANS, and TEM/HR-TEM were used to characterize these composites. The 0.5 wt% I-28/poly DCPD composite did not exhibit any neutron scattering (SANS/USANS) or X-ray scattering (SAXS) peaks to indicate the presence of ordered structures. The 0.5 wt% I-44pa/polyDCPD composite did not have an observable SAXS peak, but a very shallow peak was observed for the 1.0 wt% I-44pa samples, and a slightly larger peak was observed for the 2.0 wt% composite. No SANS peaks were observed for any of these composites. Lack of a Guinier region in USANS data indicates the presence of interacting particles.

The resulting slopes of the log−log plots of scattering intensity, $I(q)$ vs q in the low-q region for all clay/polyDCPD composites were in the range of −2.5 to −2.79 after subtracting the incoherent scattering background in SANS data. This indicates that clay tactoids exist as curved disks of various thicknesses (number of platelets varies), providing some fractal nature to disk shapes. SANS data were fitted to the stacked-disk model. Model predictions of the mean number of clay platelets per tactoid were tested by comparison to direct HR-TEM measurements of 200−450 different tactoids per sample. In the regime of low clay loadings (~0.5 wt%), the model predictions are in good agreement with direct HR-TEM measurements. However, predictions from the stacked-disk model deviate from HR-TEM results for high clay loadings (≥2 wt%). Deviation of the model at high clay loadings is possibly a consequence

Table 4. Mean Number of Tactoids Per Unit Area Measured by HR-TEM, Area Examined, and Total Tactoid Examined (Specimen Thicknesses ≈ 75−80 nm)

	I-44pa clay/polyDCPD composites		I-28 clay/polyDCPD composites		PEG-modified clay/polyDCPD composite
	0.5 wt%	2.0 wt%	0.5 wt%	2.0 wt%	0.5 wt%
mean number of tactoids per unit area (mm^2)	2.05×10^8	1.99×10^8	2.21×10^8	1.91×10^8	6.31×10^7
area examined (mm^2)	2.186×10^{-6}	2.28×10^{-6}	1.13×10^{-6}	1.614×10^{-6}	3.136×10^{-6}
total number oftactoids counted	447	454	250	309	198

of long-range interactions (important at high loadings), variation in tactoid thickness, irregular tactoid geometric shapes, and other related factors that are not taken into account by the model. Nevertheless, the stacked-disk model is a viable method to interpret SANS data from nanodispersed clay composites at low clay concentrations (~0.5 wt%). The number of tactoids (plus individual platelets) present in the composites decreased slightly as the clay loading increased from 0.5 to 2.0 wt% (when dispersed at equal sonication times). Further, the mean number of platelets per tactoid increased with clay loading. Both observations suggest that, with increased clay loading**,** the resistance to exfoliation increases and/or less energy per clay particle is delivered during sonication at higher clay loadings. The *d*-spacings between platelets in the tactoids, present after nanodispersion, are much smaller, on average (1−1.5 nm), than those in the clay particles at the start of the nanodispersion process.

Acknowledgment. The authors acknowledge the award of a Honda Fellowship to M. Yoonessi by the Bagely College of Engineering. The authors also thank Dr. Charles Glinka and Dr. Derek Ho for their helpful discussions. The Air Force Office of Scientific Research (Grant No. F49620-02-1-026-0) and the National Science Foundation (Grant No. EPS0132618) provided partial financial support for this work. The Oak Ridge National Laboratory is thanked for the use of their ORNL 10-m SAXS facility, which is sponsored by the Department of Energy under Contract No. DE-AC05-00OR22725 with Oak Ridge National Laboratory, managed by the UT-Battelle, LLC. The National Institute of Standards and Technology is thanked for Funding Proposals No. S14-13, U14-02 to conduct neutron scattering experiments. Neutron scattering experiments were supported by National Science Foundation under Agreement No. DMR-9986442.

References and Notes

(1) Kornmann, X.; Lindburg, H.; Berglund, L. A. *Polymer* **2001**, *42*, 4493−4499.
(2) LeBaron, P.C.; Pinnavaia, T. J. *Chem. Mater.* **2001**, *13*, 3760−3765.
(3) Usuki, A.; Kawasami, M.; Kojima, Y.; Okada, A.; Kurachi, T.; Kamigito, O. *J. Mater. Res.* **1993**, *8*, 1174.
(4) Usuki, A. M.; Kojima, Y.; Kawasumi, M.; Okada, A.; Fukushima, Y.; Kurauchi, T.; Kamigito, O. *J. Mater. Res.* **1993**, *8*, 1179.
(5) Kojima, Y.; Usuki, A.; Kawasumi, M.; Okada, A.; Fukushima, Y.; Kurauchi, T.; Kamigito, O. *J. Mater. Res.* **1993**, *8*, 1185.
(6) Kojima, Y.; Usuki, A.; Kawasumi, M.; Okada, A.; Kurauchi, T.; Kamigito, O. *J. Appl. Polym. Sci.* **1993**, *49*, 1259.
(7) Lan, T.; Pinnavaia, T. J. *Chem. Mater.* **1994**, *6*, 22216−2219.
(8) Chi., I. J.; Thurn-Albercht, T.; Kim, H. Ch.; Russell, T. P.; Wang, J. *Polymer* **2001**, *42*, 5947−5952.
(9) Zerda, A. S.; Lesser, A. J. *J. Polym. Sci., Part B: Polym. Phys.* **2001**, *39*, 1137−1146.
(10) Wu, J.; Lerner, M. M. *Chem. Mater.* **1993**, *5*, 835−8383.
(11) Yoonessi, M.; Toghiani, H.; Kingery, W. L.; Pittman, C. U., Jr. *Macromolecules* **2004**, *37*, 2511−2518.
(12) Ramsay, J. D. F.; Swanton, S. W.; Bunce, J. J. *J. Chem. Soc., Faraday Trans.* **1990**, *86*, 3919.
(13) Ramsay, J. D. F.; Linder, P. *J. Chem. Soc., Faraday Trans.* **1993**, *89*, 4207.
(14) Brown, A. B. D.; Clarke, S. M.; Rennie, A. R. *Prog. Colloid Polym. Sci.* **1998**, *110*, 80.
(15) Chaiko, D. J. U.S. Patent No. 051583-0262.
(16) Chaiko, D. J. 47th International SAMPE Symposium, May 12−16, 2002.
(17) Ho, D. L.; Briber, R. M.; Glinka, C. J. *Chem. Mater.* **2001**, *13*, 1923−1931.
(18) Thiyagarajan, P. *J. Appl. Cryst.* **2003**, *36*, 373−380.
(19) (a) Glinka, C., *"A SANS experiment to characterize the structure of clay platelets dispersed in water", Summer School on Neutron Scattering and Reflectometry from Submicron Structures,* NIST Center for Neutron Research, June 3−7, 2002. (b) Sears, V. F. *Neutron News* **1992**, *3*, 3, 26. (c) Bongiovanni, R., Ottewill, R. H., Rennie, A. R. *Prog. Colloid Polym. Sci.* **1991**, *84*, 299−301. (d) Choi, S. M. *SANS Experimental Methods*, 2000, (http://www.ncnr.nist.gov/programs/sans/tutorials/sans_methods.pdf). (e) Roe, R. J. *Methods of X-ray and Neutron Scattering in Polymer Science*; Oxford Press: New York, 2000; Chapter 14. (f) Lake, J. *Acta Cryst.* **1967**, *23*, 191−194. (g) Sing, M. A.; Ghosh, S. S.; Shannon, R. F. *J. Appl. Cryst.* **1993**, *26*, 787−794.
(20) Hanley, H. J. M.; Muzny, C. D.; Butler, B. D. *Langmuir* **1997**, *13*, 5276−82.
(21) Hanley, H. J. M.; Muzny, C. D.; Ho, D. L.; Glinka, C. J. *Langmuir* **2003**, *19*, 5575−5580.
(22) Ho, D. L.; Glinka, C. J. *Chem. Mater.* **2003**, *15*, 1309−1312.
(23) Guinier, A.; Fournet, G. *Small-Angle Scattering of X-Rays*; John Wiley and Sons: New York, 1955.
(24) Yue, Z. R.; Jiang, W.; Wang, L.; Gardner, S. D.; Pittman, C. U., Jr. *Carbon 37*, 1999, 1758−1796.
(25) Gardner, S. D.; He, G.; Pittman, C. U., Jr. *Carbon* **1996**, *34*, 1221−1228.
(26) (a) Xie, Y.; Sherwood, P. M. A. *Chem. Mater.* **1990**, **2**, 293. (b) Wang, T.; Sherwood, P. M. A. *Chem Mater.* **1994**, *6*, 788.
(27) Moulder, J. F.; Stickle, W. F.; Sobol, P. E.; Bomben, K. D. In *Handbook of X-ray photoelectron spectroscopy*; Chastain, J., Ed.; Perkin-Elmer Corp.: Eden Prairie, MN, 1992; p 253.
(28) (a) NIST NCNR web page for NG-3 30-m SANS small angle scattering instrument, http://www.ncnr.nist.gov/instruments/ng3sans/.
(29) a) Hammouda, B. *A Tutorial on small-angle neutron scattering*, 1995 (http://www.ncnr.nist.gov/programs/sans/tutorials/polymer_tut.pdf). (b) Kline, S. *Fundamental of Small-Angle Neutron Scattering*, 2000 (http://www.ncnr.nist.gov/programs/sans/tutorials/sans_fund.pdf). (c) Glinka, C. J. *SANS from Dilute Particle Systems*, 2000 (http://www.ncnr.nist.gov/programs/sans/tutorials/SANS_dilute_particles.pdf). (d) Choi, S. M., *SANS Experimental Methods*, 2000 (http://www.ncnr.nist.gov/programs/sans/tutorials/sans_methods.pdf). (e) Hammouda, B.; Kline, S.; Ho, D. *NG-3 30-Meter Small Angle Neutron Scattering Instrument* (http://www.ncnr.nist.gov/instruments/ng3sans/index.html.
(30) Glinka, C. J.; Barker, J.; Hammouda, B.; Krueger, S.; Moyer, J.; Orts, W. *J. Appl. Crystallogr.* **1998**, *31*, 430−445.
(31) Kline, S. *SANS Data Reduction Tutorial*, Version 4, Nov. 2001, NIST Center for Neutron Research.
(32) (a) NIST NCNR web page for Prefect-Crystal Diffractometer (PCD) for Ultrahigh-Resolution Small Angle Neutron Scattering (http://www.ncnr.nist.gov/instruments/usans/). (b) Agamalian, M.; Wignall, G. D., Triolo, R. *J. Appl. Crys.* **1997**, *30*, 345. (c) Drews, A. R.; Barker, J. G.; Glinka, C. J.; Agamalian, M. *Physica B* **1998**, *241−243*, 189−191. (d) Barker, J. Characterization of the Structure of Clay Platelets Dispersed in Water, USANS Experiment, *Summer School on Neutron Scattering and Reflectometry from Submicron Structures*, NIST Center for Neutron Research, June 3−7.
(33) Wignall, G. D.; Lin, J. S.; Spooner, S. *J. Appl. Cryst.* **1990**, *23*, 241.
(34) (a) Hendricks, R. W. *J. Appl. Cryst.* **1978**, *11*, 15−30. (b) Schelten, J.; Hendricks, R. W. *J. Appl. Cryst.* **1978**, *11*, 297−324.
(35) Russell, T. P.; Lin, J. S.; Spooner, S.; Wignall, G. D. *J. Appl. Crystallogr.* **1998**, *21*, 629.
(36) Brindley, G. W.; Brown, G. *Crystal Structures and their X-ray Identification*; Mineralogical Society: London, 1984; Vol. 5.
(37) Anderson, P. R.; Swartz, W. E. *Inorg. Chem.* **1974**, *13*, 2293.
(38) Wagner, C. D.; Passaja, D. E.; Hillery, H. F.; Kinisky, T. G.; Six, H. A.; Jansen, W. T.; Taylor, J. A. *J. Vac. Sci. Technol.* **1982**, *21*, 933−944.
(39) (a) Huang, N. P.; Csucs, G.; Emoto, K.; Nagasaki, Y.; Kataoka, K.; Textor, M.; Spencer, N. D. *Langmuir* **2002**, *18*, 1, 252−258. (b) Beamson, G.; Briggs, D. *ESCA 300 database*, 1992.
(40) Swartz, W. E.; Alfonso, R. A. *J. Electron Spectrosc. Relat. Phenom.* **1974**, *4*, 351.
(41) Barber, M.; Connor, J. A.; Guest, M. F.; Hiller, I. H.; Schwarz, M.; Stacey, M. *J. Chem. Soc., Faraday Trans. 2* **1973**, *69*, 551.
(42) Everhart, D. S.; Reilley, C. N. *Surf. Interface Anal.* **1981**, *3*, 258.
(43) Vaia, R. A.; Liu, W.; Koerner, H. *J. Polym. Sci., Part B: Polym. Phys.* **2003**, *41*, 3214.

(44) Pignon, F.; Magnin, A.; Piau, J. M.; Cabane, B.; Linder, P.; Diat, O. *Phys. Rev. E*. **1997**, *56*, 3, 3281.
(45) (a) Bare, S.; Cockcroft, J. K.; Colston, S. L.; Jupe, A. C.; Rennie, A. R. *J. Appl. Crystallogr.* **2001**, *34*, 5, 573−579. (b) Brown, A. B. D.; Clarke, S. M.; Convert, P.; Rennie, A. R. *J. Rheol*. **2000**, *44*, 2, 221−233. (c) Brown, A. B. D.; Clarke, S. M.; Rennie, A. R. *Dynamics of Complex Fluids, Proc. of the Royal Society*, Unilever Indo−UK Forum in Mater. Sci. Eng., 2nd ed., Cambridge, UK, June 24−28, 1996; pp 330−337.
(46) Kratky, O.; Porod, G. J. *J. Colloid Sci*. **1949**, *4*, 35.
(47) Higgins, J. S.; Benoit, H. C. *Polymers and Neutron Scattering*; Oxford University Press: New York, 1994.

MA048663E